



CHORUS

This is the accepted manuscript made available via CHORUS. The article has been published as:

Global stability of flowing red blood cell trains

Spencer H. Bryngelson and Jonathan B. Freund

Phys. Rev. Fluids **3**, 073101 — Published 12 July 2018

DOI: [10.1103/PhysRevFluids.3.073101](https://doi.org/10.1103/PhysRevFluids.3.073101)

Global stability of flowing red blood cell trains

Spencer H. Bryngelson¹ and Jonathan B. Freund^{1,2,*}

¹*Department of Mechanical Science & Engineering,
University of Illinois at Urbana-Champaign, Urbana, Illinois 61801, USA*

²*Department of Aerospace Engineering,
University of Illinois at Urbana-Champaign, Urbana, Illinois 61801, USA*

(Dated: June 26, 2018)

A train of red blood cells flowing in a round tube will either advect steadily or break down into a complex and irregular flow, depending upon its degree of confinement. We analyze this apparent instability, including full coupling between the viscous fluid flow and the elastic cell membranes. A linear stability analysis is constructed via a complete set of orthogonal perturbations to a boundary integral formulation of the flow equations. Both transiently ($t \rightarrow 0^+$) and asymptotically ($t \rightarrow \infty$) amplifying disturbances are identified. Those that amplify transiently have short-wavelength shape distortions that carry significant membrane strain energy. In contrast, asymptotic disturbances are primarily rigid-body-like tilts and translations. It is shown that an intermediate cell-cell spacing of about half a tube diameter suppresses long-time train instability, particularly when the vessel diameter is relatively small. Altering the viscosity ratio between the cytosol fluid within the cell and the suspending fluid is found to be asymptotically destabilizing for both higher and lower viscosity ratios. Altering the cytosol volume away from that of a nominally healthy discocyte alters the stability with complex dependence on train density and vessel diameter. Several of the observations are consistent with a switch from predominantly cell-cell interactions for dense trains and predominantly cell-wall interactions for less dense trains. Direct numerical simulations are used to verify the linear stability analysis and track the perturbation growth into a self-sustaining disordered regime.

I. INTRODUCTION

Red blood cells flowing in vessels of diameter smaller than $D \approx 8 \mu\text{m}$ are often observed in a regular cell-train formation along the vessel center-line [1–4], with each cell assuming an approximately axisymmetric bullet-like shape. However, for larger D such trains are not observed [1, 5], and the cellular flow appears far more complex [2, 6–10]. This empirical behavior has been reproduced in detailed numerical simulations [11–13]; an example in figure 1 illustrates a sensitivity of these trains to train density. In this case, the more densely packed case appears chaotic. It is known that Stokes flow can display chaos in two-dimensional mixing [14, 15], some three-dimensional flows [16–18], and N -body



FIG. 1. An example of the empirical instability of model red blood cells flowing in a uniformly spaced train. The flow is simulated using the methods of section III. A transition to apparent disorder is observed when increasing the number of cells from (a) $N = 8$ to (b) $N = 12$.

* jbfreund@illinois.edu

systems, such as a viscous suspension of spheres in a rotating cylinder [19, 20], so it is not necessarily surprising that such a transition can occur, though it is not well-characterized.

Here, we investigate the character of this transition between ordered and disordered flow, following a previous study of the stability of a two-dimensional model of capsule trains flowing in a narrow channel [21], which exhibit both transiently and asymptotically amplifying disturbances. Depending on the packing of these two-dimensional trains and channel width, the most-amplifying disturbances show an array of perturbation forms: rigid-body-like tilts, lateral translations, and compressive waves of streamwise inter-cell spacing. Although this study of two-dimensional capsule trains was motivated, in part, by observations of red-blood-cell trains, given the well-known limitations of two-dimensional models for phenomenology in three dimensions (especially in the viscous limit), we extend these methods to study the stability of geometrically and mechanically realistic red-blood cell trains. In addition to a greater number of degrees of freedom, this requires an extension of the formulation.

At the outset, we can anticipate potential differences from our previous two-dimensional capsule-train study [21]. The more rapid decay of the Stokeslet Green's function in three dimensions can be anticipated to localize interactions and yield shorter streamwise wavelengths of amplifying perturbations. The elastic resistance of the membrane is also fundamentally different. Like the two-dimensional capsule model, a red blood cell has a strong resistance to membrane dilatation [22, 23]. However, the shear modulus, which has no direct analog in the two-dimensional model, is most important, and there is only weak bending resistance [24, 25]. Red blood cells have an interior viscosity that exceeds that of the suspending plasma [26, 27]; we also consider this here, though it was not studied in the two-dimensional model.

The potential importance of cell-train behavior was discussed as motivation for the two-dimensional capsule train study [21], so it is only summarized here. Cell kinematics and the stability of the cell train can be important for cell-wall interactions via the development of a cell-free layer [28–31], margination of leukocytes and other particles [32–36], targeted drug delivery and transport [37], and in hemodynamic forces that are thought important in angiogenesis [38], development [3, 37, 39], and tumor growth [40]. Perhaps most importantly, the stability properties of cell trains might inform the design of micro-fluidic devices used to process blood cells, where a regular cell array would seem to simplify any cell-specific processing [41–46].

Our analysis is similar in spirit to that of settling rows or columns of rigid spheres [47–49], though the coupled elastic stresses of the deformable cell membranes seemingly precludes the analytically tractable formulation available in those cases. The stability of a one-dimensional droplet array has also been studied [50–52], though in that case the relative simplicity of the droplet flow system enabled analytic linearization of the governing equations. We have been unable to find such a simplified description for elastic membranes, so we have developed a numerical formulation that provides amplification rates of modal and non-modal perturbations.

In section II, we introduce the model blood vessel system in detail, and in section III we summarize the numerical methods, emphasizing the requisite generalization for this geometry. The orthogonality of the basis functions is essential, so particular emphasis is placed upon the spherical harmonic representation of the cells. The stability analysis itself is described in section IV. The formulation is similar in character to modal and non-modal analysis of shear flow at finite Reynolds numbers [53–55], though inertia is neglected here and the fully coupled fluid–structure interaction is included. Results are in section V. Transiently and asymptotically unstable perturbations and their amplification rates are determined for different vessel diameters and packing densities. The long-time evolution of these disturbances, along with random *ad hoc* perturbations for comparison, are tracked into a nonlinearly interacting and disordered flow in direct numerical simulations (DNS). Sensitivity of the train stability to cell-interior viscosity, membrane flexibility, and cell volume is also assessed, using an established nominal physiologic red-blood-cell model as a baseline case. The strain energy of the most amplifying disturbances is also quantified. Conclusions are summarized in section VI.

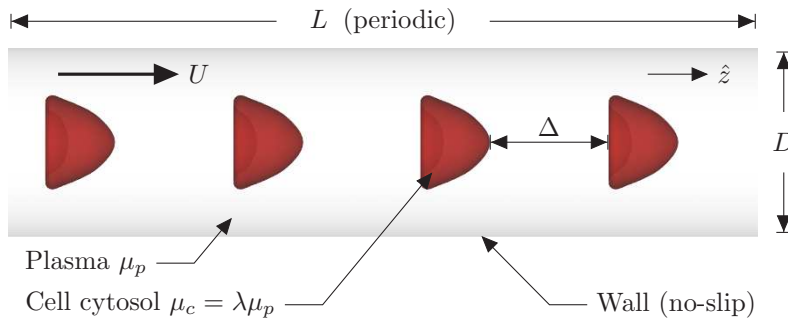


FIG. 2. The model system and boundary conditions.

II. MODEL SYSTEM

A schematic of the model microvessel is shown in figure 2. It is a rigid round tube whose diameter is taken to vary from $D = 14$ to $34 \mu\text{m}$, which includes cases for which cells are observed to flow in both ordered and apparently chaotic fashion. Model red blood cells of volume $4\pi r_o^3/3$ are initiated in their at-rest equilibrium biconcave geometry, as described elsewhere [56], with uniform spacing along the vessel center-line. This at-rest geometry is also the reference geometry for a nominal zero strain in our model, though for the relatively high strain rates we consider this is not anticipated to be consequential. A mean velocity U advects the cells. To initialize the flow configuration, flow is applied until they deform into a steadily flowing train. The stability of the train is expected to be sensitive to cell-cell spacing (see figure 1), which we quantify with $\phi \equiv r_o N/L$, where N is the number of cells and L is the periodic length of the vessel, which is varied between $\phi = 0.2$ and 0.7 . A membrane-membrane separation, Δ , is defined as the minimum streamwise separation between cells (see figure 2). Both the interior (cell cytosol) and exterior (blood plasma) fluids are modeled as Newtonian and incompressible. Most cases have plasma viscosity $\mu_p = 1.2 \times 10^{-3}$ Pas and matched cytosol viscosity $\mu_c = \mu_p$ for convenience and computation speed, however we also consider $\lambda \equiv \mu_c/\mu_p \neq 1$ in section V C. As usual, a no-slip and no-penetration condition ($\mathbf{u} = \mathbf{0}$) is enforced on the rigid vessel wall.

The red blood cell membrane elastic resistance is described using a Skalak constitutive model with independent shear and dilatation moduli [11, 57], for which the strain energy is

$$W = \frac{E_s}{8} (I_1^2 + 2I_1 - 2I_2) + \frac{E_d}{8} I_2^2, \quad (1)$$

where $E_s = 4.2 \times 10^{-6}$ N/m is the shear modulus, $E_d = 67.7 \times 10^{-6}$ N/m (or $C = E_d/E_s = 16.1$ in terms of the often cited Skalak dilatation coefficient) is the relatively large dilatation modulus, enforcing the near incompressibility of actual red cell membranes, and $I_{1,2}$ are the usual strain invariants. We confirm that the instability amplification rates of section V B vary by less than 2% upon doubling E_d , which confirms that the train stability is insensitive to this specific choice. Bending is resisted through a linear isotropic model [11], which yields bending moment

$$\mathbf{M} = -E_b(\boldsymbol{\kappa} - \boldsymbol{\kappa}^R), \quad (2)$$

where $E_b = 1.8 \times 10^{-19}$ N m is the bending modulus (with value based upon measurements [56]), $\boldsymbol{\kappa}$ is the second fundamental form of the surface (the covariant component of the Riemann curvature tensor), and $\boldsymbol{\kappa}^R$ is the corresponding second fundamental form of the reference biconcave shape.

Together, these parameters can form a capillary number $Ca \equiv \mu U/E_s$, which quantifies advection to relaxation times and serves as a measure of flow strength. The effect of Ca on train-stability is assessed in section V D. The Reynolds number of microcirculatory flow is generally small: for $r_o = 2.8 \mu\text{m}$, a fast flow velocity $U = 2.9 \times 10^{-3}$ m/s, plasma viscosity $\mu_p = 1.2 \times 10^{-3}$ Pas, and mass density $\rho = 10^3$ kg/m³, $Re \equiv \rho U r_o/\mu_p \lesssim 0.01$. Thus, inertia is

neglected. Though this model includes significant simplifications relative to actual physiological blood flow, it is able to quantitatively reproduce, for example, the effective viscosity of blood flow in narrow tubes [6, 11].

III. NUMERICAL METHODS

The flow is represented with a standard boundary integral formulation [58–60], for which the x_i -direction velocity component u_i is described implicitly by

$$u_i(\mathbf{x}_o) = \frac{2}{1+\lambda} u_i^\infty(\mathbf{x}_o) - \frac{1}{1+\lambda} \frac{1}{4\pi\mu_p} \int_{\mathcal{S}} G_{ij}(\mathbf{x} - \mathbf{x}_o) \Delta\sigma_j(\mathbf{x}) dS(\mathbf{x}) - \frac{1-\lambda}{1+\lambda} \frac{1}{4\pi} \int_{\mathcal{S}} T_{ijk}(\mathbf{x} - \mathbf{x}_o) u_j(\mathbf{x}) n_k(\mathbf{x}) dS(\mathbf{x}). \quad (3)$$

In (3), \mathbf{x}_o is a point on a cell surface, \mathcal{S} is the union of all surfaces such as those shown in figure 2, $\Delta\boldsymbol{\sigma}$ is the net surface traction vector acting on the fluid due to the deformation of the membrane, and \mathbf{G} and \mathbf{T} are the so-named Stokeslet and stresslet Green's functions of the viscous-flow equations [59]. Here, a uniform $\mathbf{u}^\infty = \{0, 0, \hat{U}\}$ is the mean velocity in the $L_d \times L_d \times L$ rectangular computational domain, which is required by our triply-periodic Green's function formulation [11]; we use $L_d = D + 0.5r_o$, and \hat{U} thus sets the flow strength. This \hat{U} does not exactly match U in the vessel, since for the periodic-domain boundary integral formulation there is also flow outside the vessel. Thus, U is determined by subtracting the flow rate outside the vessel from the total flow rate $L_d^2 \hat{U}$ and dividing by the cross-sectional area of the vessel [11]. The mean velocity in the vessel U thus depends on \hat{U} and the effective viscosity of the suspension within the vessel, though for the cases we consider ($U/D > 50$ /s) the effective viscosity is shear-rate insensitive [61]. In our computations we use $\hat{U} = 2.3 \times 10^{-3}$ m/s, and U/\hat{U} varies only from 1.244 to 1.256. Further, in section VD we demonstrate that the growth rates we compute are only weakly (approximately logarithmically) sensitive to Ca , and thus U . So, for our purposes, we will use a nominal $U = 1.25\hat{U} = 2.875 \times 10^{-3}$ m/s for non-dimensionalization.

Cell membranes shapes are discretized with spherical harmonics as

$$\mathbf{x}^{(j)}(\theta, \psi) = \sum_{n=0}^{M-1} \sum_{m=0}^n \tilde{P}_n^m(\sin\theta) \left[\mathbf{a}_{nm}^{(j)} \cos m\psi + \mathbf{b}_{nm}^{(j)} \sin m\psi \right], \quad (4)$$

where $\mathbf{x}^{(j)}$ is the surface position of cell j , \tilde{P}_n^m are normalized Legendre polynomials, and $\mathbf{a}_{nm}^{(j)}$ and $\mathbf{b}_{nm}^{(j)}$ are the coefficients of the expansion. This spectral discretization is advantageous since it both requires relatively few modes to accurately describe the cell shape and facilitates a nondissipative dealiasing method for nonlinear stability [11]. The orthogonality of the spherical harmonic basis is also utilized in the stability formulation of section IV.

Reported calculations use $M = 12$, though $3M$ are carried for approximately dealiased nonlinear evaluations and quadrature; the instability amplification rates of section V vary by only 1% for $M = 16$. The spherical harmonic coefficients are represented compactly as $\vec{\mathbf{s}} = \{\mathbf{a}_{nm}^{(j)}, \mathbf{b}_{nm}^{(j)}\}$, where $j = 1, \dots, N$ indicates the cell. The $n \geq m$ spectral expansion coefficient indices in (4) yield a combined $\vec{\mathbf{s}}$ vector of length $3NM^2$. For any cell, the corresponding discrete surface points are $\vec{\mathbf{x}}^{(j)} = \{\mathbf{x}^{(j)}(\theta_l, \psi_m)\}$ as computed by (4), where $\theta_l \in (0, \pi)$ for $l = 1, \dots, M$ are the colatitudinal Gauss points and $\psi_m \in [0, 2\pi)$ for $m = 1, \dots, 2M$ are the uniformly spaced longitudinal points [62]. The discrete spherical harmonic transform pair for all cells can be expressed compactly as

$$\vec{\mathbf{x}} = \mathbf{B}\vec{\mathbf{s}} \quad \text{and} \quad \vec{\mathbf{s}} = \tilde{\mathbf{B}}\vec{\mathbf{x}}, \quad (5)$$

where matrices \mathbf{B} and $\tilde{\mathbf{B}}$ represent (4) applied at all the collocation points.

The surface tractions $\Delta\boldsymbol{\sigma}$ complete the local force and torque balances for the membrane surface, and the spatial derivatives used to evaluate them are computed analytically via the spherical harmonic expansion [11, 63]. The boundary integrals of (3) are then evaluated using the quadrature scheme consistent with the collocation points $\vec{\mathbf{x}}$,

except for close interactions, for which a nearly-singular formulation of the integrands is used [11]. The resulting linear system is evaluated approximately but accurately by a particle-mesh-Ewald (PME) algorithm generalized for Stokes flow [11, 63, 64].

The vessel wall is represented by 6588 triangular elements, and is uniformly stretched for varying D and L . A single-layer potential, based on \mathbf{G} , is used to enforce the no-slip condition by solving for the required surface traction on the wall with a GMRES algorithm [11, 65].

Once the velocity $\vec{\mathbf{u}}$ on the cells is computed from the discretized form of (3), the cell membranes advance according to

$$\frac{d\vec{\mathbf{x}}}{dt} = \vec{\mathbf{u}}(\vec{\mathbf{x}}) \quad \left(\text{or} \quad \frac{dx_i^{(j,k)}}{dt} = u_i^{(j,k)}(\vec{\mathbf{x}}) \quad \text{for} \quad i = 1, 2, 3; \quad j = 1, \dots, N; \quad k = 1, \dots, M^2 \right). \quad (6)$$

For the direct numerical simulations, which we report to complement the stability analysis, (6) is integrated using a first-order explicit method with time step $\Delta t = 0.0014 r_o / U$. The base states are insensitive to this choice, with the growth rates of section VB varying less than 0.1% upon halving Δt .

Since the fluids are incompressible, there should be no change in cell volume, though even small errors can accumulate over long simulation times, which is corrected through adjustment of the cell membrane in its normal direction [11]. The reported simulations require adjustments of less than $10^{-5} r_o$ per time step, and the stability analysis is independent of this procedure.

IV. STABILITY ANALYSIS FORMULATION

A. Measure of configurational stability

We consider geometric displacements, $\vec{\varepsilon}_x(t) \equiv \vec{\mathbf{x}}(t) - \vec{\mathbf{x}}_b(t)$, where $\vec{\mathbf{x}}_b$ is the uniformly advecting base flow configuration, described in detail in section VA. However, their representation requires a generalization of the approach we used in the two-dimensional case, where Fourier modes described the capsule shapes [21]. Since the Fourier transform is unitary, describing disturbances with physical points ($\vec{\varepsilon}_x$) sufficed and was convenient. However, the spherical harmonic transformation has an overdetermined physical-to-harmonic ($\vec{\mathbf{x}}$ to $\vec{\mathbf{s}}$) transformation. Thus, it is more direct to formulate a disturbance $\vec{\varepsilon}$ to the corresponding spherical harmonic coefficients $\vec{\mathbf{s}}$:

$$\vec{\varepsilon}(t) \equiv \vec{\mathbf{s}}(t) - \vec{\mathbf{s}}_b(t). \quad (7)$$

A generalization of Parseval's theorem indicates that the norms of $\vec{\mathbf{x}}$ and $\vec{\mathbf{s}}$ only differ by a constant factor [66], so $\vec{\varepsilon}$ provides a useful measure of perturbation amplitude,

$$\|\vec{\varepsilon}\|^2 = \sum_{i=1}^{3NM^2} (\varepsilon_i)^2, \quad (8)$$

with $\|\vec{\varepsilon}_x\|^2 = \|\vec{\varepsilon}\|^2 / 2.2$. This measure is not unique, however, and is not expected to be for such a complex system [54]. For example, a metric based upon constant flow energies is often used for finite- Re flows, though it is not implemented here since even zero-strain-energy disturbances can be amplifying.

B. Linearization

With the numerical evaluation of $\tilde{\mathbf{u}}(\vec{\mathbf{x}})$ available, the linear system governing small perturbations can be determined by evaluating $\tilde{\mathbf{u}}(\vec{\mathbf{x}} + \mathbf{B}\vec{\delta})$ for each of a complete basis of perturbations $\vec{\delta}$. An expansion yields

$$\tilde{\mathbf{u}}(\vec{\mathbf{x}} + \mathbf{B}\vec{\delta}) = \tilde{\mathbf{u}}(\vec{\mathbf{x}}) + \mathbf{C}\mathbf{B}\vec{\delta} + \mathcal{O}(\|\mathbf{B}\vec{\delta}\|^2), \quad (9)$$

where \mathbf{C} is an unknown linear coefficient matrix. Multiplying (9) by $\tilde{\mathbf{B}}$ to put it in terms of the expansion coefficients and retaining only the linear contribution yields

$$\mathbf{A}\vec{\delta} = \tilde{\mathbf{B}}\tilde{\mathbf{u}}(\vec{\mathbf{x}} + \mathbf{B}\vec{\delta}) - \tilde{\mathbf{B}}\tilde{\mathbf{u}}(\vec{\mathbf{x}}), \quad (10)$$

where $\mathbf{A} = \tilde{\mathbf{B}}\mathbf{C}\mathbf{B}$ is the square matrix that represents all first-order coupling of the base state to the perturbation. Each column of \mathbf{A} is computed by perturbing the corresponding spherical harmonic mode $k \in \{1, \dots, M^2\}$ in one of the coordinate directions $i \in \{1, 2, 3\}$ for each cell $j \in \{1, \dots, N\}$ and calculating $\tilde{\mathbf{B}}\tilde{\mathbf{u}}(\vec{\mathbf{x}} + \mathbf{B}\vec{\delta})$. Thus, following the notation in (6), for each column only the $(i; j, k)$ component of $\vec{\delta}$ is perturbed by δ , such that

$$\delta_p^{(q,r)} = \begin{cases} \delta & \text{for } p = i, q = j, r = k \\ 0 & \text{otherwise,} \end{cases} \quad (11)$$

which yields the (i, j, k) column of \mathbf{A} as

$$A_{ip}^{(j,k,q,r)} = \frac{\left[\tilde{\mathbf{B}}\tilde{\mathbf{u}}(\vec{\mathbf{x}} + \mathbf{B}\vec{\delta}) - \tilde{\mathbf{B}}\tilde{\mathbf{u}}(\vec{\mathbf{x}}) \right]_p^{(q,r)}}{\delta} \quad \text{for } p = 1, 2, 3; \quad q = 1, \dots, N; \quad r = 1, \dots, M^2. \quad (12)$$

Repeating this for each spherical harmonic coefficient and coordinate direction constructs the full $3NM^2 \times 3NM^2$ matrix \mathbf{A} . We note that only $3M^2$ independent evaluations of the nonlinear system are required to construct the full \mathbf{A} , since the flow is periodic and thus \mathbf{A} is block-periodic; in practice the computational cost of this procedure is comparable to $3M^2$ time steps of the flow system (6). For 8 cells at this resolution, this requires approximately 5 hours on a modern workstation. Since the spherical harmonic modes are mutually orthogonal, this \mathbf{A} describes the full linear dynamics of the system. This is confirmed in section V for $\delta = 10^{-3}$, which is used in most of the calculations. Once \mathbf{A} is constructed, the initial evolution of any sufficiently small disturbance $\vec{\epsilon}$ follows from (9) as

$$\frac{d\vec{\epsilon}}{dt} = \mathbf{A}\vec{\epsilon}, \quad (13)$$

which has exact solution $\vec{\epsilon}(t) = [\exp \mathbf{A}t]\vec{\epsilon}_o$ for initial condition $\vec{\epsilon}(0) = \vec{\epsilon}_o$.

C. Eigensystem and verification

Since \mathbf{A} is non-normal, in general it will not have a complete set of orthogonal eigenvectors. As a result, transient growth is possible and the largest real eigenvalue does not necessarily correspond to the maximum growth rate at all times [54, 67]. However, the eigensystem of \mathbf{A} nevertheless indicates the $t \rightarrow \infty$ growth of small perturbations [53]. For $\vec{\lambda}(\mathbf{A})$ eigenvalues of \mathbf{A} , the spectral abscissa of the system is its largest real component, which bounds asymptotic growth,

$$\alpha \equiv \max \left\{ \text{Re} \left[\vec{\lambda}(\mathbf{A}) \right] \right\}. \quad (14)$$

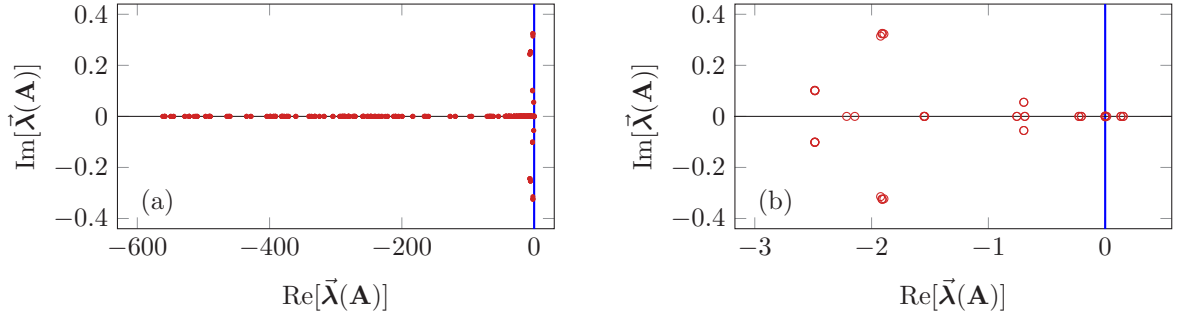


FIG. 3. Eigenvalues of \mathbf{A} for a two-cell case with $D = 10r_o$, $\phi = 0.2$, and viscosity ratio $\lambda = 5$. The same data are shown in (a) and (b) with different scales.

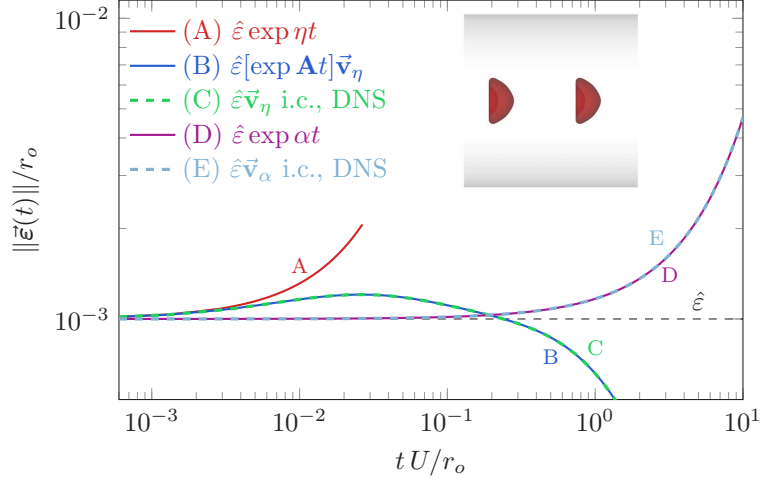


FIG. 4. Behavior and verification for a case with $N = 2$, $D = 10r_o$, $\phi = 0.2$, viscosity ratio $\lambda = 5$, and initial disturbance magnitude $\hat{\varepsilon} = 10^{-3}r_o$.

The corresponding eigenvector \vec{v}_α , when added to the base flow \vec{x} , will amplify as $e^{\alpha t}$ for $t \rightarrow \infty$. Similarly, the transient amplification rate for $t \rightarrow 0^+$ is bounded by the nominal numerical abscissa [54, 67],

$$\eta \equiv \max \left\{ \text{Re} \left[\vec{\lambda} \left(\frac{\mathbf{A} + \mathbf{A}^T}{2} \right) \right] \right\}, \quad (15)$$

with \vec{v}_η the corresponding eigenvector of $(\mathbf{A} + \mathbf{A}^T)/2$.

Example eigenvalues of \mathbf{A} are shown in figure 3. Most have $\text{Re}[\vec{\lambda}(\mathbf{A})] < 0$, and thus are asymptotically stable, as expected for a viscous system. However, three eigenvalues do have positive real components, so the system is asymptotically unstable.

A comparison of the linear predictions with \mathbf{A} and corresponding direct numerical simulations (DNS) is shown in figure 4. While $\hat{\varepsilon} \exp \eta t$ bounds transient growth for $t \rightarrow 0^+$, it is clear from the DNS result in figure 4 that amplification ceases after a relatively short time and the perturbation decays below the most asymptotically amplifying disturbance \vec{v}_α by $t = 0.2U/r_o$. This non-monotonic behavior matches the matrix exponential $\hat{\varepsilon}[\exp \mathbf{A}t]\vec{v}_\eta$, which verifies its prediction for linear behavior. The growth of \vec{v}_α and its linear prediction also match.

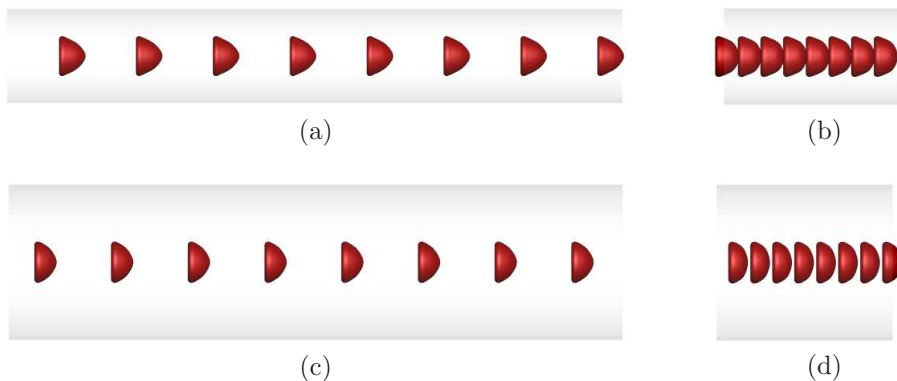


FIG. 5. Example base flow configurations: (a) $D = 6r_o$, $\phi = 0.2$, (b) $D = 6r_o$, $\phi = 0.7$, (c) $D = 10r_o$, $\phi = 0.2$, (d) $D = 10r_o$, $\phi = 0.7$.

V. RESULTS

A. Base cases

Flows in different tube diameters D and train packings ϕ are first simulated to establish the base state, which is taken to be converged when the maximum wall-normal velocity of any cell collocation point is less than $10^{-4}U$. Example base-flow configurations are shown in figure 5. We focus on trains with $N = 8$ cells as shown; doubling N affects the amplification rates we identify by less than 1%, consistent with the corresponding short streamwise wavelength perturbations we find.

B. Matched viscosity ratio $\lambda = 1$

Several cases with $\lambda = 1$ are discussed in this section. The effect of $\lambda \neq 1$ on the train stability is investigated in section V C.

1. Asymptotic behavior

The dependence of α on D and ϕ is shown in figure 6 (a). For $\phi = 0.2$ the system is unstable with $\alpha \approx 10^{-1}U/r_o$ for all diameters D , though the modestly smaller α for larger D suggests that increased cell-wall interaction is weakly destabilizing. For this α and flow rate, such a perturbation would amplify by a factor of 10 upon flowing about $30r_o$ downstream. The more packed cases with $\phi = 0.7$ have similar amplification, also with $\alpha \approx 10^{-1}U/r_o$ for all D . However, for intermediate ϕ , growth is suppressed. For $D \lesssim 10r_o$ and $0.4 \lesssim \phi \lesssim 0.55$ we have $\alpha < 10^{-3}U/r_o$, which suggests relative stability. Unfortunately, the numerical approximations are such that it is not possible to distinguish $\alpha < 10^{-3}U/r_o$ from true $\alpha = 0$ marginal stability. The $\delta = 10^{-3}r_o$ used to construct \mathbf{A} , as formulated in section IV, limits this discrimination. Smaller δ , better converged flow configurations, and higher spatial resolution would all be necessary to determine these α more precisely. This would be challenging, and is fortunately unimportant for our conclusions. For $\alpha = 10^{-3}U/r_o$, the corresponding streamwise distance required for a disturbance to grow from $\hat{\varepsilon} = 10^{-3}r_o$ to r_o is $\Delta z \gtrsim U \log(\hat{\varepsilon}^{-1})/\alpha \approx 1.4 \times 10^5 r_o$. Thus, these cases are deemed marginally stable for our purposes; their exponential amplification is more than 100 times slower than that of the most-amplifying disturbances we find for other cases.

Example eigenvectors are visualized in figure 6 (b). Those associated with the $\phi = 0.2$ cases appear as tilts of the cells, which was also seen for some two-dimensional capsule trains [21]. In contrast, the eigenvectors for the $\phi = 0.7$

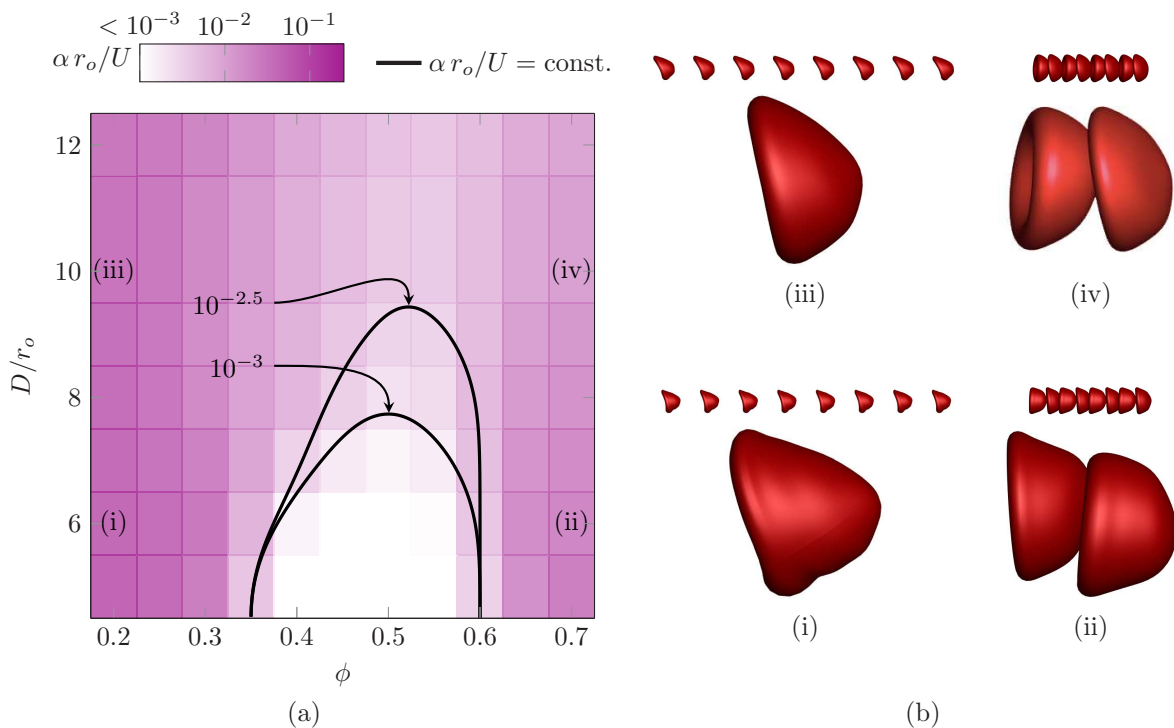


FIG. 6. (a) Spectral abscissa amplification α for the full range of D and ϕ . The constant α curves suggest a region of apparent marginal stability (see text). (b) Example \vec{v}_α for (i) $D = 6r_o, \phi = 0.2$, (ii) $D = 6r_o, \phi = 0.7$, (iii) $D = 10r_o, \phi = 0.2$, and (iv) $D = 10r_o, \phi = 0.7$, as labeled in (a). The wrinkled appearance is due to the $\vec{s} + 10\vec{v}_\alpha$ magnification used to visualize the small perturbation.

cases are wave-like, though with only two cells per wavelength, and involve a combination of capsule translations and tilts.

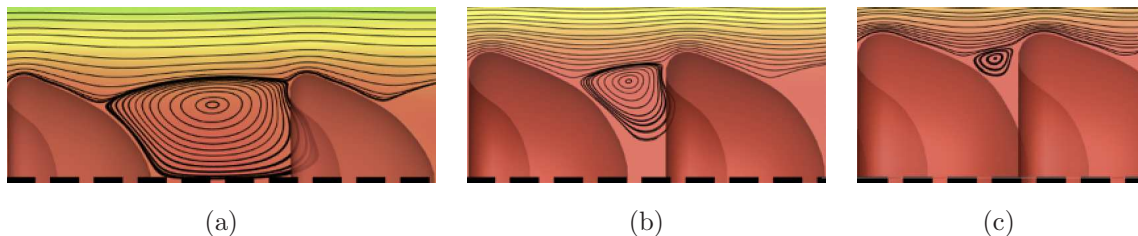


FIG. 7. Streamlines relative to the cell-attached-frame for $D = 6r_o$ for (a) an example unstable loosely packed $\phi = 0.3$ case, (b) a marginally stable $\phi = 0.5$ case, and (c) an unstable densely packed $\phi = 0.7$ case. The $---$ line is the tube center-line.

The streamlines in a cell-fixed frame for different base states are shown in figure 7. For the $D = 6r_o$ cases shown, the train is marginally stable for $0.4 \lesssim \phi \lesssim 0.55$ and unstable otherwise. The streamlines for $\phi \lesssim 0.4$, which show a prominent recirculation regions that join on the tube center-line. This flow instability is a uniform rotation of the cells, as was seen in figure 6 (b). However, for $0.4 \lesssim \phi \lesssim 0.55$ the flow is qualitatively different, and it stagnates near the tube center-line, and no such linear instability is found. For $\phi \gtrsim 0.6$, which is also unstable though with a 2-cell zig-zag pattern, the cells are close and the recirculation is limited to a small region adjacent to the cells.

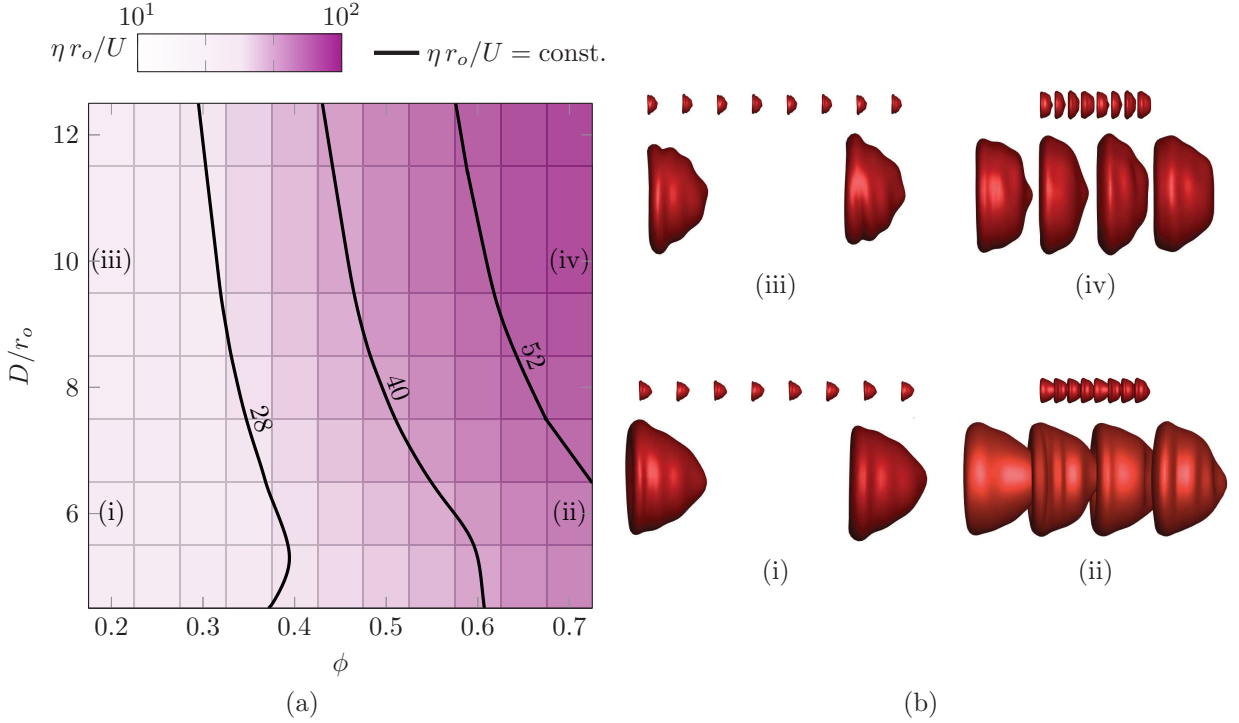


FIG. 8. (a) Numerical abscissa η . Solid black lines are curves of constant η for values as labeled. (b) Example $\vec{\mathbf{v}}_\eta$ for (i) $D = 6r_o$, $\phi = 0.2$, (ii) $D = 6r_o$, $\phi = 0.7$, (iii) $D = 10r_o$, $\phi = 0.2$, and (iv) $D = 10r_o$, $\phi = 0.7$, visualized as $\vec{\mathbf{s}} + 10\vec{\mathbf{v}}_\eta$. Again, the exaggerated wrinkled appearance is due to the magnification used to visualize the small perturbation.

2. Transient behavior

The corresponding $t \rightarrow 0^+$ most amplifying growth rates η are shown in figure 8 (a). These vary by about a factor of four over this range, generally increasing with larger D and ϕ . This general behavior is similar to that for short, two-dimensional capsule trains, though unlike those cases it is insensitive to the streamwise-periodic length of the flow. The associated perturbations are visualized in figure 8 (b) and all have a wave-like character. For cases with $\phi = 0.2$ a wavelength includes just two cells and the disturbances are asymmetric, while for the more packed $\phi = 0.7$ cases they include four cells per wavelength and are asymmetric for $D = 6r_o$ and axisymmetric for $D = 10r_o$. These forms are similar in character to some of the (more extensively mapped) disturbances found for two-dimensional capsule trains [21], though again without the apparent dependence on domain length found in that configuration.

Although the transient growth rates of figure 8 are large, such that the magnitude of the associated disturbance would increase by a factor of 10 after traveling a streamwise distance of only $0.4D$, this rapid growth is transient. Figure 9 shows the evolution of the most-amplifying transient and asymptotic disturbances. The transient growth is consistent with the linear prediction for short times, but quickly decays with $\|\vec{\mathbf{e}}\| < \hat{\epsilon}$ by the time the cells have advected about one tube diameter D . These cases were selected in part because of their relatively large η , as seen in figure 8 (a), yet the failure of such disturbances, even with relatively a large initial disturbance magnitude $\hat{\epsilon} = 0.1r_o$, to trigger nonlinear interactions suggests a subservient role of the transient mechanism. In the analogous two-dimensional configuration, many transiently growing disturbances were found to amplify to the point of nonlinear saturation [21]. No such persistent transient growth was found here for red blood cells.

We quantify the character of the most-amplifying disturbances by their spherical harmonic deformation spectrum [6]:

$$E_n = \frac{1}{N} \sum_{j=1}^N \sum_{m=0}^n (|\mathbf{a}_{nm}^{(j)}|^2 + |\mathbf{b}_{nm}^{(j)}|^2), \quad (16)$$

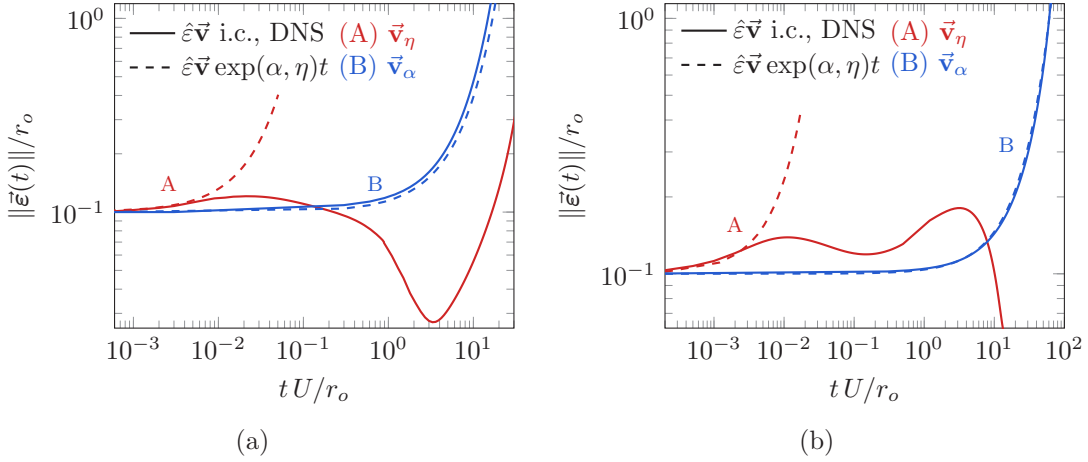


FIG. 9. DNS evolution and linear predictions for \vec{v}_α and \vec{v}_η , are shown with relatively large $\hat{\epsilon} = 0.1r_o$ initial disturbance for cases (a) $D = 10r_o$, $\phi = 0.2$ and (b) $D = 10r_o$, $\phi = 0.7$. Linear predictions of \vec{v}_α remain good for long times as expected, though transient disturbances \vec{v}_η undergo rapid decay.

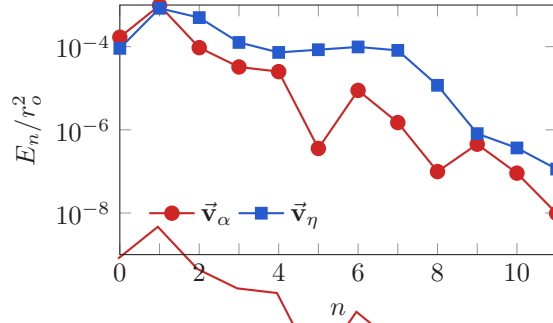


FIG. 10. Cell-averaged deformation spectra (16) for \vec{v}_α and \vec{v}_η for $D = 10r_o$ and $\phi = 0.7$.

where $\mathbf{a}_{nm}^{(j)}$ and $\mathbf{b}_{nm}^{(j)}$ are defined in (4). In figure 10, we see the \vec{v}_α spectrum decays faster, indicating that \vec{v}_α is smoother than \vec{v}_η . The corresponding low-order moment contributions of the disturbance to the flow at a distance are therefore expected to be longer range. In contrast, high-order contributions primarily entail disturbance to the surface curvature that can be anticipated to decay rapidly [68]. In section V G we will see that \vec{v}_η also carry significant strain energy.

3. Nonlinear saturation

Direct numerical simulations are used in particular cases to track the linear amplification into subsequent disordered flow, presumably reflecting nonlinear dynamics. Example results are shown in figure 11, where they are compared with their respective linear growth rates α . The linear theory and full simulations for the $\hat{\epsilon}\vec{v}_\alpha$ initial condition match closely until $\|\vec{\epsilon}_x(t)\| \approx 0.5r_o$ for $\phi = 0.7$ and $\|\vec{\epsilon}_x(t)\| \approx 5r_o$ for $\phi = 0.2$. Visualizations suggest that this larger value for $\phi = 0.2$ is due to the large streamwise displacements that must occur for stronger cell-cell interactions in this case. For comparison, the time evolution of an *ad hoc* perturbation, $\vec{v}_{\text{ad hoc}}$, is also shown. This disturbance is constructed by randomly displacing each cell, without deformation, in each coordinate direction. The *ad hoc* disturbance amplifies slower than \vec{v}_α for both cases, requiring about 4.3 and 2.7 times longer to evolve to $\|\vec{\epsilon}_x(t)\|/r_o = 1$ for $\phi = 0.2$ and 0.7, respectively.

The transition to disordered flow is visualized in figure 12 for the $\phi = 0.7$ case. We see that the initial perturbation

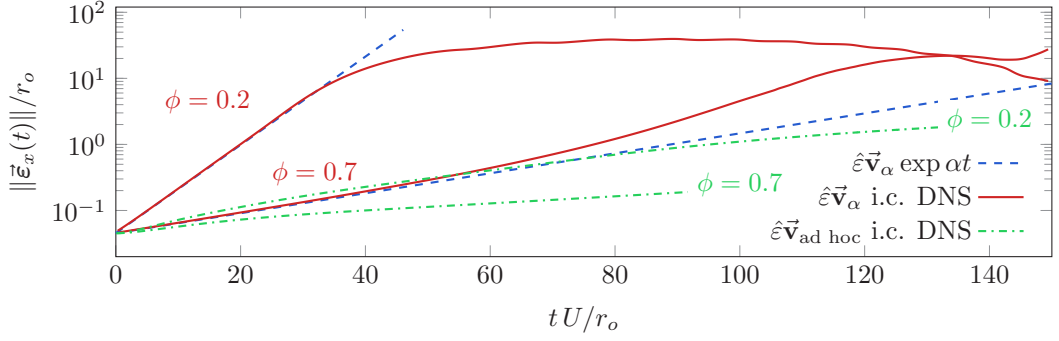


FIG. 11. $\|\vec{\epsilon}_x(t)\|$ for \vec{v}_α and an *ad hoc* disturbance $\vec{v}_{ad hoc}$ (see text) with $\hat{\epsilon} = 0.1r_o$ and corresponding DNS for $D = 10r_o$ and $\phi = 0.2$ and 0.7 , as indicated.

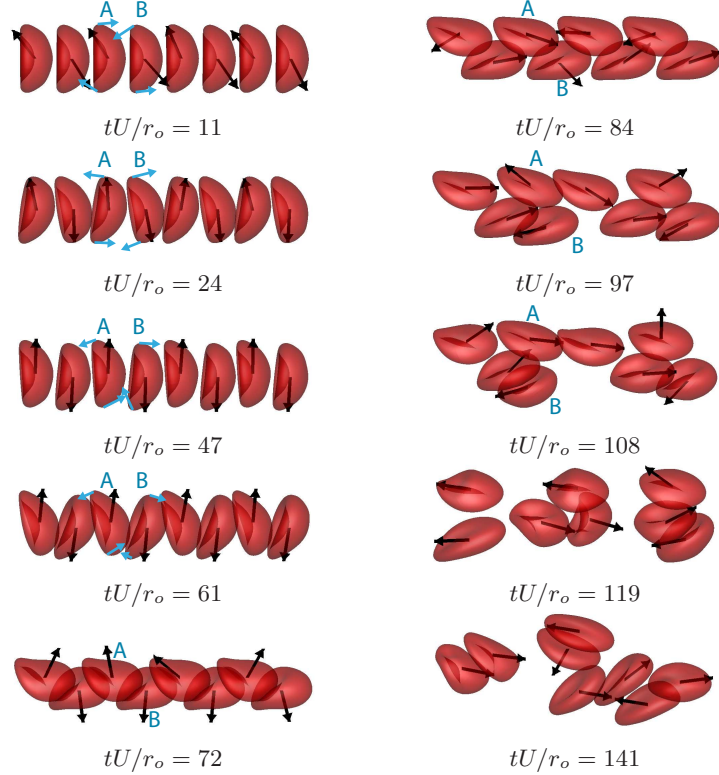


FIG. 12. The time evolution and subsequent train breakup of \vec{v}_α for $D = 10r_o$ and $\phi = 0.7$. The velocities of the cell centroids relative to that of the initial mean flow, $\hat{\mathbf{u}}' \equiv \mathbf{u}' - \mathbf{u}^\infty$, are shown as black vectors. Two initially adjacent cells are labeled as A and B to illustrate the relative cell motion. For $tU/r_o \leq 61$ blue vectors show the surface velocity relative to the centroid, $\hat{\mathbf{u}}_s \equiv \mathbf{u} - \hat{\mathbf{u}}'$. Walls are not shown, though they can be seen in the base state visualization in figure 5 (d). The times were selected to illustrate the flow development.

tilts and displaces the cells with a wavelength of two cells, bringing them closer to the tube wall. The retarded flow near the wall slows and rotates the cells. This can be seen for $tU/r_o \leq 61$, as cells A and B rotate in opposite directions; this structure repeats for all cells. The resulting staggered cell-train is similar to that observed in some narrow tubes [69]. This differs from the collective long wavelength behavior exhibited by the analogous two-dimensional capsule trains [21]. Around $tU/r_o \approx 72$ the rotation of the cells is sufficiently large that the cells take on slipper-like shapes with alternating orientation, such as those commonly observed in both numerical simulations [70–72] and experiments [4, 73, 74]. This every-other-cell structure then separates and eventually breaks up into an apparently

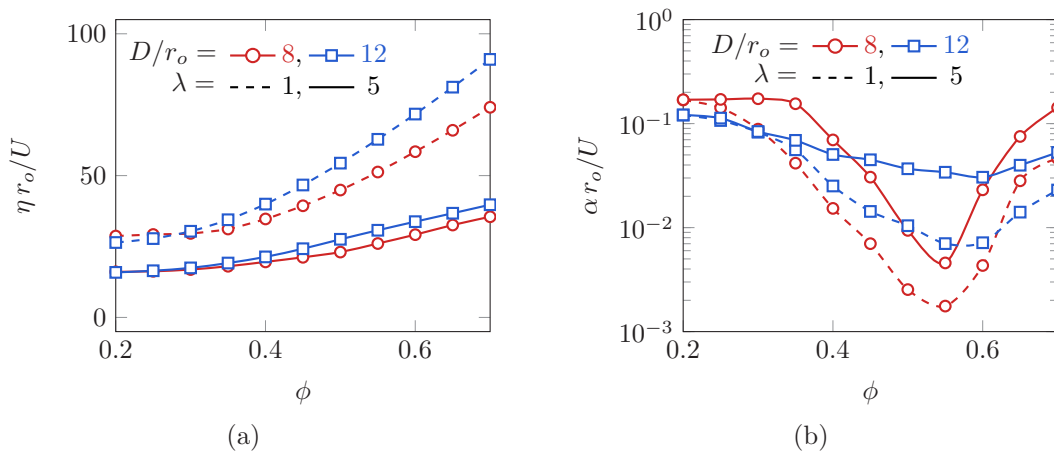


FIG. 13. (a) Numerical (η) and (b) spectral (α) abscissa for $\lambda = 1$ and 5 and $D = 8r_o$ and $12r_o$ as labeled versus ϕ .

random behavior for $tU/r_o \gtrsim 97$, presumably by a secondary instability mechanism.

C. Effect of viscosity ratio λ

A healthy, newly-formed red blood cell is thought to have a cytosol viscosity about $\lambda \approx 5$ times that of blood plasma [26, 27]. Here, we consider both the $\lambda = 5$ nominally physiological case, as well as more extreme variations, including some unphysiologic, yet interesting, cases with $\lambda < 1$. The base configurations of figure 5 still apply.

The effects of λ on η and α are shown in figure 13. Transient amplification η is decreased by about factor of 2, from $\lambda = 1$ to $\lambda = 5$, for all ϕ considered. In section VG we show that the shape-deformations associated with transient growth entail significant elastic strain energy. We expect viscosity to increasingly counter elastic relaxation for larger λ . In contrast, α is larger for $\lambda = 5$ than $\lambda = 1$, except for cases with $\phi \lesssim 0.3$, for which α is insensitive to this change in λ . For larger ϕ , elevated $\lambda = 5$ increases α by about a factor of 4 compared to the corresponding $\lambda = 1$ case. We will confirm subsequently that this is generally the case for increasing λ .

The cell interior viscosity can change through disease, deoxygenation [75, 76] and cell aging [77, 78], and ex vivo the exterior viscosity can be readily changed by altering the suspending fluids. Thus, we also consider cases with $\lambda = 0.1$ to 100. Example α are shown in figure 14. For $\phi = 0.2$, increasing λ from 1 to 20 only increases α by about 10% for the cases shown. For $\lambda \gtrsim 20$, α approximately plateaus and it appears that the cells effectively behave as rigid-bodies as far as their stability is concerned. When λ is decreased from $\lambda = 1$, the train is also more unstable, though the relative change in α is small. However, when the cell train is more densely packed, as for $\phi = 0.7$ in figure 14 (b), α is many times more sensitive to λ . Again, a non-monotonic behavior is observed, with $\lambda \approx 1$ the most stable. An approximate plateau in α is also observed in this case for $\lambda \gtrsim 20$.

It is known that the viscosity ratio can have a marked impact on the cell-scale dynamics of the flow, particularly in regard to the tumbling and tank-treading motions of the cells. We quantify these dynamics for the most-amplifying perturbations following a straightforward procedure [6]. The rigid-body-like tumbling motion of the cells is quantified via the rotation rate vector $\boldsymbol{\omega}$ based upon their best-fit ellipsoids. The time rate of change of any vector \mathbf{e} on this ellipsoid is

$$\dot{\mathbf{e}} = \boldsymbol{\omega} \times \mathbf{e}. \quad (17)$$

We take \mathbf{e} as the principal axes, which are given by the eigenvectors of \mathbf{M} , which has components

$$M_{ij} = \frac{1}{A_s} \int_S x'_i x'_j dS, \quad (18)$$

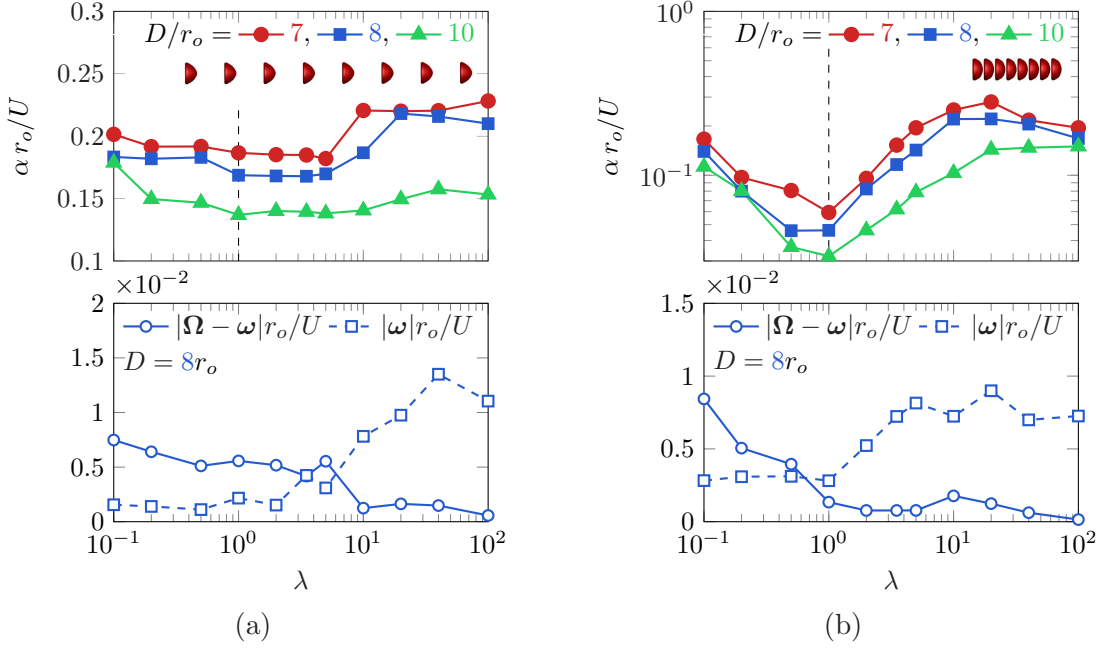


FIG. 14. Amplification factor α and tank-treading and tumbling metrics for varying λ and (a) $\phi = 0.2$ and (b) $\phi = 0.7$.

where A_s is the surface area of the cell and \mathbf{x}' is the membrane surface position relative to the cell centroid. Taking the cross-product of each side of (17) with \mathbf{e} and summing over the three principal unit vectors \mathbf{e}_i gives

$$\left[3\mathbf{I} - \sum_{i=1}^3 \mathbf{e}_i \mathbf{e}_i \right] \cdot \boldsymbol{\omega} = \sum_{i=1}^3 \mathbf{e}_i \times \dot{\mathbf{e}}_i, \quad (19)$$

where \mathbf{I} is the rank 3 identity tensor. We compute $\dot{\mathbf{e}}$ using the $t \rightarrow 0$ DNS for disturbance $\hat{\varepsilon} \vec{\mathbf{v}}_\alpha$; (19) is then solved for $\boldsymbol{\omega}$.

Tank treading, which is membrane rotation without change in the basic cell shape, is quantified as the deviation of $\boldsymbol{\omega}$ from the instantaneous membrane rotation rate $\mathbf{\Omega}$, defined by

$$\mathbf{R} \cdot \mathbf{\Omega} = \int_S \mathbf{v}' \times \mathbf{x}' dS(\mathbf{x}), \quad (20)$$

where \mathbf{v}' is the local membrane velocity relative to the cell centroid, and \mathbf{R} is the so-called inertia tensor:

$$\mathbf{R} = A_s [\mathbf{I} \text{tr} \mathbf{M} - \mathbf{M}]. \quad (21)$$

These tank treading $|\mathbf{\Omega} - \boldsymbol{\omega}|$ and tumbling $|\boldsymbol{\omega}|$ metrics are shown for select cases in figure 14. For both $\phi = 0.2$ and 0.7 , tumbling $|\boldsymbol{\omega}|$ increases with λ until $\lambda \gtrsim 20$. The switch to predominantly tumbling kinematics is consistent with the λ insensitive behavior of α , and suggests that the increased growth rates with λ for $\lambda \leq 20$ are associated with this increased tumbling. This concurs with the visualizations of figure 12, which show how the cells move out of the uniform train primarily through rotation. With decreasing λ from $\lambda = 1$ the rate of tank-treading $|\mathbf{\Omega} - \boldsymbol{\omega}|$ increases, as expected for cells with less viscous interiors. However, the tumbling for these cases is relatively unchanged.

D. Effect of flow strength (Ca)

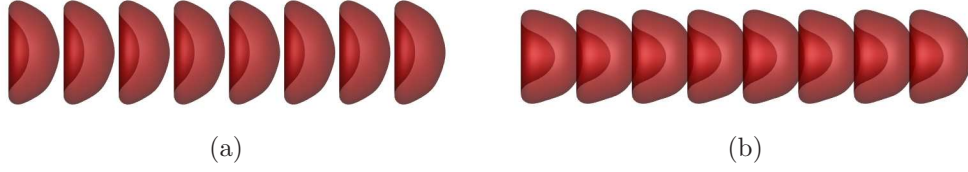


FIG. 15. Cell trains with $D = 8r_o$ for the (a) smallest $Ca = 0.4$ and (b) largest $Ca = 20.5$ we consider.

The flow strength $Ca \equiv \mu U/E_s$ is varied from 0.4 to 20.5 to understand its affect on the train stability away from the $Ca = 0.66$ of the previous sections. Example baseline configurations for the Ca extremes are visualized in figure 15.

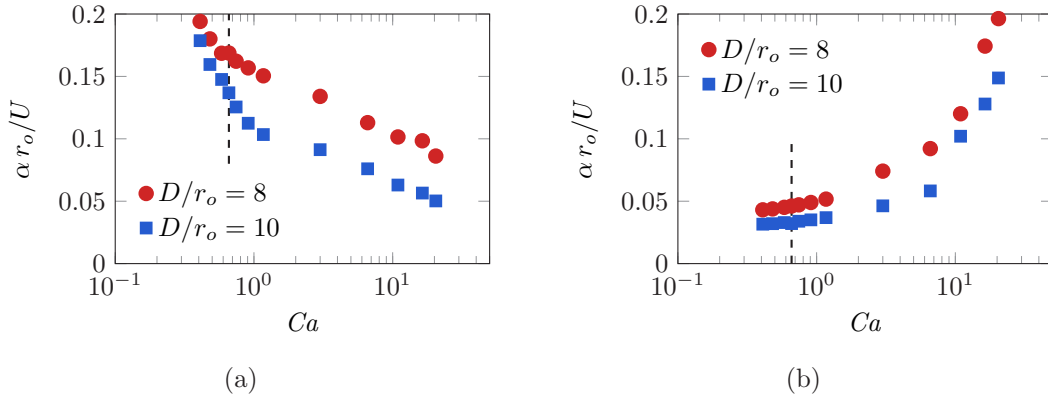


FIG. 16. Dependence of amplification rate α on flow strength Ca for $\lambda = 1$ and (a) $\phi = 0.2$ and (b) $\phi = 0.7$. The dashed lines indicate the $Ca = 0.66$ of most other cases.

The effect on asymptotic stability is shown in figure 16. For $\phi = 0.2$, α generally decreases with Ca , and by a factor of about two from $Ca = 1$ to $Ca = 10$ for both tube diameters. There is also a decrease of $0.11r_o$ in distance from the cell membrane to the tube wall for both D shown over this range of Ca . We anticipate this change in α to be primarily due to cell-wall interactions, rather than cell-cell interactions. This effect will be quantified directly in the next section.

This is in contrast to the more densely-packed $\phi = 0.7$ cases, which are more unstable for increasing Ca , as seen in figure 16 (b). This result is consistent with that of two-dimensional capsule trains [21]. Larger Ca leads to more deformed and streamwise-extended cells, which in turn leads to smaller cell-cell spacing Δ . Increasing ϕ for fixed Ca also increases α (see section VB 1), which is consistent with the trend shown here. For the cases of figure 16 (b), we also see that the rate at which α increases with Ca is matched by the rate at which the effective membrane-membrane separation Δ decreases. Thus, increased cell-cell interaction due to smaller cell-cell spacing would seem to result in a more unstable cell train. We will see a consistent increase in α with decreasing Δ in the next section, where we also investigate the effect of changes in cell shape on train stability. There we also quantify this cell-cell interaction directly.

E. Effect of cell volume

Diseased or infected red blood cells also often have modified shapes. Sickle or anemic cells have reduced volume [79], whereas elliptocytes and spherocytes have increased volume [80, 81], so their stability in a train might be especially

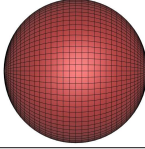
v	Visualization	v	Visualization
0.40		0.72	
0.47		0.81	
0.55		0.90	
0.61		0.95	
0.64		1.0	

FIG. 17. Equilibrium shapes for reduced volume v . The reference healthy red blood cell shape used in previous sections has $v = 0.64$.

important in microfluidic devices designed to identify, analyze, or process them. It is also known that such diseased or transformed cells can alter confined flows [31, 82]. More generally, artificial cell-like capsules can be manufactured with a wide range of volumes [83]. Here, we investigate the role of the cell volume V relative to its maximum V_o on the train stability by varying the reduced volume away from the baseline $v \equiv V/V_o = 0.64$ of the previous sections, which was set to approximately match that of a healthy red blood cell [84].

The equilibrium shapes are visualized in figure 17 for $v = 0.4$ to 1. For $v < 0.61$, an *ad hoc* finite intra-cellular repulsion prevents the membrane from self-intersecting while the base shape is forming [11], though this repulsion is not needed to maintain the equilibrium shape, so the shapes in figure 17 are independent of it. Example base-flow configurations for the v extremes are visualized in figure 18.

We note that it is not obvious how to compare cases, since deflation and inflation maintains the same centroid-to-centroid spacing, though with different membrane-to-membrane spacing Δ . Since their shapes depend in complex fashion upon v , Ca , and D/r_o , we choose to retain the definition $\phi \equiv r_o N/L$ for making comparisons, aware that membrane-to-membrane spacing generally decreases with increasing v .

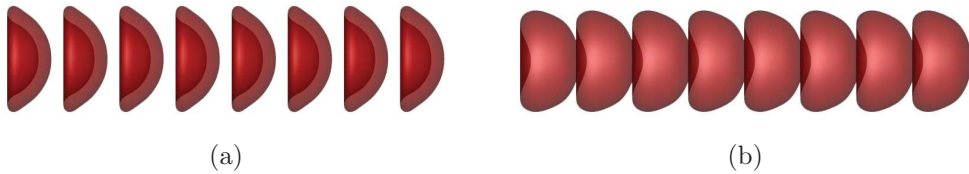


FIG. 18. Base configurations of cell trains for $D = 8r_o$ and $\phi = 0.7$: (a) $v = 0.40$ and (b) $v = 0.86$.

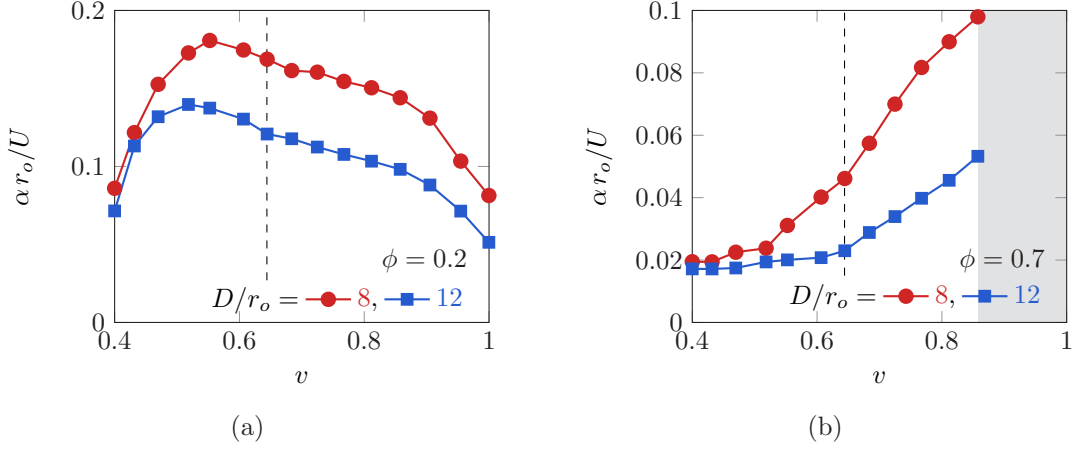


FIG. 19. Maximum $t \rightarrow \infty$ amplification α for varying D/r_o , v , and (a) $\phi = 0.2$ and (b) $\phi = 0.7$. All cases have $\lambda = 1$. Vertical dashed lines indicate the nominal healthy red blood cell $v = 0.64$ used in most other cases. In (b), the shaded regime $v > 0.86$ indicates states that cannot form a train without overlapping.

Results for the asymptotic amplification are shown in figure 19. The sparse cases of $\phi = 0.2$ are most unstable for $v \approx 0.55$ for $D = 8r_o$ and $v \approx 0.52$ for $D = 12r_o$, and are more stable for both larger and smaller v . Cases with relatively large v can be anticipated to be less unstable, since their orientation becomes less important. Rotations, such as those seen in section VB, are thus less consequential. For the more densely packed $\phi = 0.7$ cases, α monotonically increases with v . For larger v , the membrane-to-membrane separation Δ (see figure 2) decreases, which will increase hydrodynamic coupling between neighboring cells. This was also shown to be asymptotically destabilizing in sections VB and VC for healthy red blood cell shapes, and anticipated as the mechanism of densely packed train breakup in section VD. We also see α is smaller for larger D for all cases; this is again consistent with the results of section VD, as cases with larger D have less deformed cells, and thus smaller Δ and decreased cell-cell coupling.

F. Cell-cell and cell-wall interactions

To quantify the effect of cell-cell and, consequentially, cell-wall hydrodynamic interactions on the train stability, we alter \mathbf{A} such that the nearest \tilde{N} cell-cell interactions are removed, both upstream and downstream. This new matrix $\tilde{\mathbf{A}}$ is formed by zeroing the appropriate $3M^2 \times 3M^2$ blocks in \mathbf{A} . The associated asymptotic growth rate without the \tilde{N} nearest neighbor interactions is then

$$\tilde{\alpha} \equiv \max \left\{ \text{Re} \left[\tilde{\lambda}(\tilde{\mathbf{A}}) \right] \right\}. \quad (22)$$

Thus, $\tilde{N} = 0$ recovers $\tilde{\mathbf{A}} = \mathbf{A}$ and $\tilde{\alpha} = \alpha$, since all interactions are included; for $N = 8$ and $\tilde{N} = 4$ only the interactions with periodic images of the cell itself and with the walls are included.

In figure 20, we see that for $\phi = 0.7$ all cases are strongly stabilized by removing the nearest cell-cell interactions ($\tilde{N} = 1$), and this is most significant for larger Ca and v , both of which reduce Δ . This is consistent with nearest neighbor interactions being the proximate mechanism of instability. For $\phi = 0.7$, $\tilde{\alpha}$ can decrease by as much as a factor of 1000 for $\tilde{N} = 1$. For $\phi = 0.2$ a similar trend is seen, though with only a factor 1.4 decrease in $\tilde{\alpha}$. In these cases, the wall and its effect on the cell shape itself are most important.

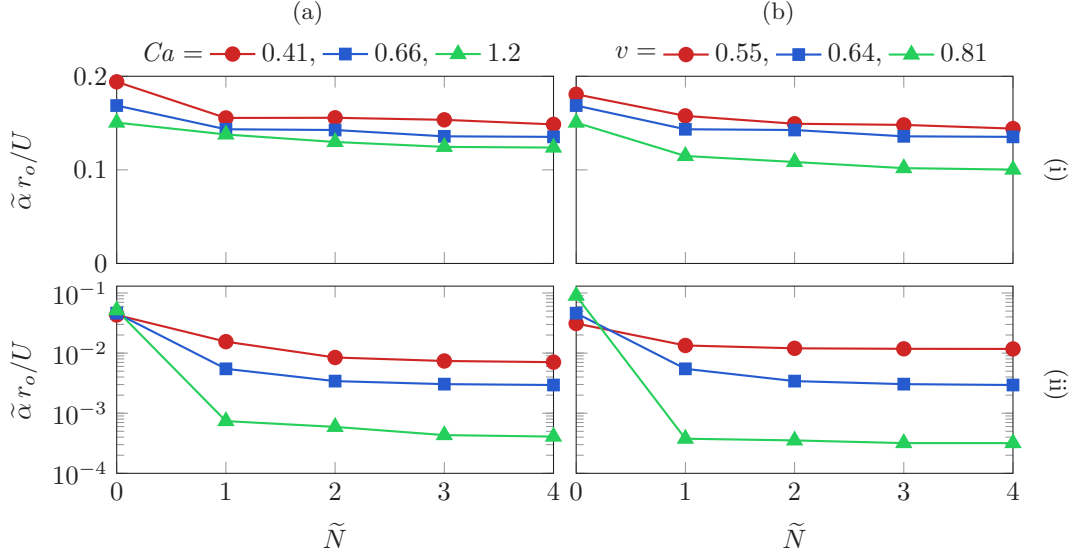


FIG. 20. Modified growth rate $\tilde{\alpha}(\tilde{N})$ for $D = 8r_o$, (a) varying Ca and $v = 0.64$, and (b) varying v and $Ca = 0.66$. Both (i) $\phi = 0.2$ and (ii) $\phi = 0.7$ are shown.

D/r_o	ϕ	W'_α	$W'_\eta = W'_{\eta,s} + W'_{\eta,d} + W'_{\eta,b}$			
6	0.2	1.13×10^{-2}	2.48	0.43	2.01	0.04
6	0.7	4.29×10^{-3}	2.42	0.74	1.52	0.16
10	0.2	9.16×10^{-3}	1.95	0.59	1.31	0.05
10	0.7	3.95×10^{-3}	4.91	0.43	4.25	0.23

TABLE I. Strain energy for most-amplifying transient, W'_η , and asymptotic W'_α perturbation for a $\lambda = 1$ cell train of select vessel diameters D/r_o and packing fractions ϕ . All W' are computed for $\hat{\varepsilon} = 10^{-3}r_o$ and nondimensionalized by r_o , U , and μ .

G. Perturbation strain energy

Our stability measure of section IV is based upon geometric displacement of the cell membranes. However, this formulation does not afford a direct assessment of the perturbation strain energy, which for cell j is

$$W_j = \int_{C_j} \left[\frac{E_s}{8} (I_1^2 + 2I_1 - 2I_2) + \frac{E_d}{8} I_2^2 + \frac{E_b}{2} (b - b^R)_i^2 \right] dS, \quad (23)$$

where C_j is the surface of the cell, $I_{1,2}$ are the usual strain invariants, b are the principal curvatures [11], and superscript R denotes the reference shape [11, 85]. The contributions of shear, dilatation, and bending resistance to W are denoted as W_s , W_d , and W_b , respectively. The cell-averaged perturbation strain-energy is

$$W' = \frac{r_o}{\hat{\varepsilon}N} \sum_{i=1}^N (W_i - W_i^B), \quad (24)$$

where W_i^B is the strain energy of a cell in the base flow configuration.

Example results are listed in table I. The most-amplifying transient disturbances carry markedly more strain energy than asymptotic ones, matching the results for two-dimensional capsule trains of our previous study [21]. Further, for the cases of table I all transiently unstable disturbances, not just the most amplifying, have $W' > 0.6$. This suggests that the transient instabilities generally require significant membrane deformation. In contrast, the asymptotic modes have strain energy comparable to the linearization approximation made in our stability formulation. In all cases, the dilatation part $W'_{\eta,d}$ of the transient strain energy disturbance is largest and the bending part $W'_{\eta,b}$ is smallest, likely

owing to their relatively large and small moduli, $E_d r_o^2 \gg E_b$. The smallest W'_η in table I provides an estimate of the strain energy required to form the most-amplifying transient disturbances. Its dimensional value, $\widehat{W}'_\eta \gtrsim 6 \times 10^{-18}$ J, is more than 10^3 times larger than $kT = 4.3 \times 10^{-21}$ J for $T = 37^\circ$ C. Thus, only disturbances with $\hat{\varepsilon} < 10^{-3} r_o$ are expected to arise via thermal fluctuations. This is notable, since the results of section V B 2 predict that even $\hat{\varepsilon} = 0.1 r_o$ is insufficient to trigger a nonlinear transition. Thus, it seems that transiently amplifying disturbances are unlikely to form spontaneously with sufficient amplitude to trigger nonlinear dynamics. The most amplifying asymptotic modes are not so constrained.

VI. SUMMARY AND ADDITIONAL DISCUSSION

For some parameters, the train is found to be $t \rightarrow \infty$ marginally stable, at least to within the precision of our calculations. Indeed the cell-train packing ϕ of these cases matches the cell-cell separation observed for cells in small capillaries [86–88], which have $0.3 \lesssim \phi \lesssim 0.6$. For larger tube diameters or sparse or dense cell-cell spacing in narrow tubes, many cases are found to be asymptotically unstable, with the corresponding most amplifying disturbances being cell rotations and translations. This is in contrast to the two-dimensional capsule trains studied previously, where the most asymptotically amplifying disturbances were qualitatively different and depended upon the flow description.

Transiently amplifying disturbances were identified for all cases considered. Many of these amplify thousands or more times faster than the corresponding asymptotically amplifying modes. However, since they require significant strain energy to form they are unlikely to occur without significant input to the system. Even then, the subsequent growth is so brief that they are not expected to grow to the point of significant nonlinearity. This is in contrast to the two-dimensional capsule trains of a previous study, for which the corresponding transient modes were able to trigger a nonlinear mechanism for relatively small perturbations [21].

Larger cell-interior viscosity increases the amplification rate until $\lambda \approx 20$ where the rate of amplification appears to saturate, seeming to reach a rigid-body-like behavior in this high-viscosity limit. Changing the reduced volume of the cells leads to a similarly rich behavior on the train stability: deflating the cells increases cell train stability for the nearly jammed $\phi = 0.7$ cases we considered, whereas a more unstable train was predicted for $\phi = 0.2$. Transient instabilities we identified took the form of cell membrane deformations, which corresponded to finite strain energy disturbances, compared to the nearly zero strain energy disturbance of the asymptotically amplifying modes.

These results suggest that the train packing fraction, tube diameter, and cell interior viscosity and volume can be selected to mediate instability of the train, and thus provide a route to the improved design of microdevices. Specifically, our results predict that cell-trains with $0.4 \lesssim \phi \lesssim 0.6$, $D \lesssim 10 r_o$, and $\lambda \approx 1$ will flow a minimum streamwise distance of $10^5 r_o$ before a small disturbance can amplify 10^3 times. Deviations from these ranges leads to decreased train stability, which we quantified for certain parameter choices.

Finally, we observed that asymptotically amplifying disturbances are rigid-body-like rotations and translations of the cells, rather than deformations of the cell membranes (as have been identified in other capsule flows, e.g. steady extension [89, 90]). A consequence is that such low-order disturbances are amenable to suppression through flow control techniques [91–93]. Thus, a microfluidic device utilizing such a control mechanism might process otherwise unstable (as identified here) cell trains sequentially. Further, the structure of instabilities, such as we identify, might be exploited in conjunction with more complicated geometries, such as bifurcating vessels.

ACKNOWLEDGMENTS

This work was supported in part by the National Science Foundation under Grant No. CBET 13-36972.

[1] R. Skalak and P. I. Branemark, “Deformation of red blood cells in capillaries,” *Science* **164**, 717–719 (1969).

- [2] A. R. Pries and T. W. Secomb, “Rheology of the microcirculation,” *Clin. Hemorheol. Microcirc.* **29**, 143–148 (2003).
- [3] J. B. Freund, “Numerical simulations of flowing blood cells,” *Annu. Rev. Fluid Mech.* **46**, 67–95 (2014).
- [4] G. Tomaiuolo, M. Simeone, V. Martinelli, B. Rotoli, and S. Guido, “Red blood cell deformation in microconfined flow,” *Soft Matter* **5** (2009).
- [5] T. W. Secomb, R. Skalak, N. Ozkaya, and J. F. Gross, “Flow of axisymmetric red blood cells in narrow capillaries,” *J. Fluid Mech.* **163**, 405–423 (1986).
- [6] J. B. Freund and M. M. Orescanin, “Cellular flow in a small blood vessel,” *J. Fluid Mech.* **671**, 466–490 (2011).
- [7] J. L. McWhirter, H. Noguchi, and G. Gompper, “Ordering and arrangement of deformed red blood cells in flow through microcapillaries,” *New J. Phys.* **14**, 085026 (2012).
- [8] P. Gaehtgens, C. Duhressen, and K. H. Albrecht, “Motion, deformation, and interaction of blood cells and plasma during flow through narrow capillary tubes,” *Blood Cells* **6**, 799–812 (1980).
- [9] T. M. Griffith, “Temporal chaos in the microcirculation,” *Cardiovascular Research* **31**, 342–358 (1996).
- [10] K. D. Barclay, G. A. Klassen, and C. Young, “A method for detecting chaos in canine myocardial microcirculatory red cell flux,” *Microcirculation* **7**, 335–346 (2000).
- [11] H. Zhao, A. H. G. Isfahani, L. Olson, and J. B. Freund, “A spectral boundary integral method for micro-circulatory cellular flows,” *J. Comp. Phys.* **229**, 3726–3744 (2010).
- [12] P. Bagchi and R. M. Kalluri, “Rheology of a dilute suspension of liquid-filled elastic capsules,” *Phys. Rev. E* **81** (2010).
- [13] D. A. Fedosov, M. Dao, G. E. Karniadakis, and S. Suresh, “Computational biorheology of human blood flow in health and disease,” *Ann. Biomed. Eng.* **42**, 368–387 (2013).
- [14] H. Aref, “Stirring by chaotic advection,” *J. Fluid Mech.* **143**, 1–21 (1984).
- [15] J. M. Ottino, *The Kinematics of Mixing: Stretching, Chaos and Transport* (Cambridge University Press, 1989).
- [16] K. Bajer and H. K. Moffatt, “On a class of steady confined Stokes flows with chaotic streamlines,” *J. Fluid Mech.* **212**, 337–363 (1990).
- [17] H. A. Stone, A. Nadim, and S. H. Strogatz, “Chaotic streamlines inside drops immersed in steady Stokes flows,” *J. Fluid Mech.* **232**, 82–46 (1991).
- [18] D. Kroujiline and H. A. Stone, “Chaotic streamlines in steady bounded three-dimensional Stokes flows,” *Physica D* **130**, 105–132 (1999).
- [19] I. M. Jánosi, T. Tél, D. E. Wolf, and J. A. C. Gallas, “Chaotic particle dynamics in viscous flows: The three-particle Stokeslet problem,” *Phys. Rev. E* **56**, 2858–2868 (1997).
- [20] T. Mullin, Y. Li, C. Del Pino, and J. Ashmore, “An experimental study of fixed points and chaos in the motion of spheres in a Stokes flow,” *IMA J. App. Math.* **70**, 666–676 (2005).
- [21] S. H. Bryngelson and J. B. Freund, “Capsule-train stability,” *Phys. Rev. Fluids* **1** (2016).
- [22] E. A. Evans and R. Waugh, “Osmotic correction to elastic area compressibility measurements on red cell membrane,” *Biophys. J.* **20**, 307–313 (1977).
- [23] C. D. Eggleton and A. S. Popel, “Large deformation of red blood cell ghosts in a simple shear flow,” *Phys. Fluids* **10**, 1834–1845 (1998).
- [24] E. Evans, “Bending elastic modulus of red blood cell membrane derived from buckling instability in micropipet aspiration tests,” *Biophys. J.* **43**, 27–30 (1983).
- [25] M. Dao, C. T. Lim, and S. Suresh, “Mechanics of the human red blood cell deformed by optical tweezers,” *J. Mech. Phys. Solids* **51**, 2259–2280 (2003).
- [26] L. Distenfass, “Internal viscosity of the red cell and a blood viscosity equation,” *Nature* **219**, 956–958 (1968).
- [27] G. R. Cokelet and H. J. Meiselman, “Rheological comparison of hemoglobin solutions and erythrocyte suspension,” *Science* **162**, 275–277 (1968).
- [28] C. Alonso, A. R. Pries, O. Kiesslich, D. Lerche, and P. Gaehtgens, “Transient rheological behavior of blood in low-shear tube flow: velocity profile and effective viscosity,” *Am. J. Physiol. Heart Circ. Physiol.* **268**, 25–32 (1995).
- [29] M. Soutani, Y. Suzuki, and N. Maeda, “Quantitative evaluation of flow dynamics of erythrocytes in microvessels: influence of erythrocyte aggregation,” *Am. J. Physiol. Heart Circ. Physiol.* **268**, H1959–H1965 (1995).
- [30] S. Kim, P. K. Ong, O. Yalcin, M. Intaglietta, and P. C. Johnson, “The cell-free layer in microvascular blood flow,” *Biorheology* **46**, 181–189 (2009).
- [31] S. H. Bryngelson and J. B. Freund, “Buckling and its effect on the confined flow of a model capsule suspension,” *Rheol. Acta* **55**, 451–464 (2016).
- [32] J. C. Firrell and H. H. Lipowsky, “Leukocyte margination and deformation in mesenteric venules of ram,” *Am. J. Physiol. Heart Circ. Physiol.* **225**(6), 1667–1674 (1989).

- [33] J. B. Freund, “Leukocyte margination in a model microvessel,” *Phys. Fluids* **19** (2007).
- [34] H. Zhao and E. S. G. Shaqfeh, “Shear-induced platelet margination in a microchannel,” *Phys. Rev. E* **83** (2011).
- [35] A. Kumar, R. G. Henriquez Rivera, and M. D. Graham, “Flow-induced segregation in confined multicomponent suspensions: effects of particle size and rigidity,” *J. Fluid Mech.* **738**, 423–462 (2014).
- [36] R. G. Henriquez Rivera, K. Sinha, and M. D. Graham, “Margination regimes and drainage transition in confined multicomponent suspensions,” *Phys. Rev. Lett.* **114** (2015).
- [37] J. B. Freund, J. Goetz, K. Hill, and J. Vermot, “Fluid flows and forces in development: functions, features and biophysical principles,” *Development* **139**, 1229–1245 (2012).
- [38] T. W. Secomb, J. P. Alberding, R. Hsu, M. W. Dewhurst, and A. R. Pries, “Angiogenesis: An adaptive dynamic biological patterning problem,” *PLoS Comput. Biol.* **9** (2013).
- [39] F. Boselli, J. B. Freund, and J. Vermot, “Blood flow mechanics in cardiovascular development,” *Cellular and Molecular Life Sciences* **72**, 2545–2559 (2015).
- [40] P. Koumoutsakos, I. Pivkin, and F. Milde, “The fluid mechanics of cancer and its therapy,” *Annu. Rev. Fluid Mech.* **45**, 325–355 (2013).
- [41] C. Galligan, J. Nichols, E. Kvam, P. Spooner, R. Gettings, L. Zhu, and C. M. Puleo, “Mesoscale blood cell sedimentation for processing millilitre sample volumes,” *Lab on a Chip* **15**, 3274–3277 (2015).
- [42] N. Xiang and Z. Ni, “High-throughput blood cell focusing and plasma isolation using spiral inertial microfluidic devices,” *Biomed Microdevices* **17** (2015).
- [43] J. Choi, J. Hyun, and S. Yang, “On-chip extraction of intracellular molecules in white blood cells from whole blood,” *Scientific Reports* (2005).
- [44] M. Abkarian, M. Faivre, R. Horton, K. Smistrup, and C. A. Best-Popescu, “Cellular-scale hydrodynamics,” *Biomed. Mater.* **3** (2008).
- [45] M. Toner and D. Irimia, “Blood-on-a-chip,” *Ann. Rev. Biomed. Eng.* **7**, 77–103 (2005).
- [46] J. Kim, M. Massoudi, J. F. Antaki, and A. Gandini, “Removal of malaria-infected red blood cells using magnetic cell separators: a computational study,” *Appl. Math. Comput.* **218** (2012).
- [47] J. M. Crowley, “Viscosity-induced instability of a one-dimensional lattice of falling spheres,” *J. Fluid Mech.* **45**, 151–159 (1971).
- [48] L. M. Hocking, “The behavior of clusters of spheres falling in a viscous fluid,” *J. Fluid Mech.* **20**, 129 (1964).
- [49] S. L. Goren, “Resistance and stability of a line of particles moving near a wall,” *J. Fluid Mech.* **132**, 185–196 (1983).
- [50] T. Beatus, T. Tlustý, and R. Bar-Ziv, “Phonons in a one-dimensional microfluidic crystal,” *Nature Physics* **2**, 743–748 (2006).
- [51] J. Fleury, U. D. Schiller, S. Thutupalli, G. Gompper, and R. Seemann, “Mode coupling of phonons in a dense one-dimensional microfluidic crystal,” *New J. Phys.* **16**, 063029 (2014).
- [52] S. Kuriakose and P. Dimitrakopoulos, “Deformation of an elastic capsule in a rectangular microfluidic channel,” *Soft Matter* **9**, 4284–4296 (2013).
- [53] P. J. Schmid and D. S. Henningson, *Stability and Transition in Shear Flows* (Springer Science and Business Media, 2012).
- [54] P. J. Schmid, “Nonmodal stability theory,” *Annu. Rev. Fluid Mech.* **39**, 129–162 (2007).
- [55] M. Zhang, F. Martinelli, J. Wu, P. J. Schmid, and M. Quadrio, “Modal and non-modal stability analysis of electrohydrodynamic flow with and without cross-flow,” *J. Fluid Mech.* **770**, 319–349 (2015).
- [56] C. Pozrikidis, “Axisymmetric motion of a file of red blood cells through capillaries,” *Phys. Fluids* **15** (2005).
- [57] R. Skalak, A. Tozeren, P. R. Zarda, and S. Chien, “Strain energy function of red blood cell membranes,” *Biophysical J.* **13**, 245 (1973).
- [58] S. Kim and S. J. Karrila, *Microhydrodynamics: Principles and Selected Applications* (Butterworth-Heinemann, Boston, 1991).
- [59] C. Pozrikidis, *Boundary Integral and Singularity Methods for Linearized Viscous Flow* (Cambridge University Press, 1992).
- [60] J. M. Rallison and A. Acrivos, “A numerical study of the deformation and burst of a viscous drop in an extensional flow,” *J. Fluid Mech.* **89**, 191–200 (1978).
- [61] A. R. Pries, D. Neuhaus, and P. Gaehtgens, “Blood viscosity in tube flow: dependence on diameter and hematocrit,” *Am. J. Physiol.* **263** (1992).
- [62] J. C. Adams and P. N. Swartztrauber, *SPHEREPACK 2.0: A model development facility*, Tech. Rep. NCAR/TN-436-STR (NCAR, 1997).
- [63] J. B. Freund and H. Zhao, “A fast high-resolution boundary integral method for multiple interacting blood cells,” in *Hydrodynamics of Capsules and Biological Cells*, edited by C. Pozrikidis (Chapman and Hall/CRC, Boca Raton, FL, 2010)

pp. 71–111.

- [64] D. Saintillan, E. Darve, and E. S. G. Shaqfeh, “A smooth particle-mesh Ewald algorithm for Stokes suspension simulations: the sedimentation of fibers,” *Phys. Fluids* **17** (2005).
- [65] Y. Saad and M. Schultz, “A generalized minimal residual algorithm for solving nonsymmetric linear systems,” *SIAM J. Sci. Stat. Comput.* **7**, 856–869 (1985).
- [66] O. L. Colombo, *Numerical methods for harmonic analysis on the sphere*, Scientific Report 7 (United States Air Force, 1981).
- [67] L. Trefethen and M. Embree, *Spectra and Pseudospectra: The Behavior of Nonnormal Matrices and Operators* (Princeton: Princeton Univ. Press, 2005).
- [68] J. Gounley and Y. Peng, “Shape recovery of elastic capsules from shear-flow induced deformation,” *Commun. Comput. Phys.* **16**, 56–74 (2014).
- [69] V. Claveria, O. Aouane, M. Thiebaud, M. Abkarian, G. Coupier, C. Misbah, T. John, and C. Wagner, “Clusters of red blood cells in microcapillary flow: hydrodynamic versus macromolecule induced interaction,” *Soft Matt.* **12**, 8235–8245 (2016).
- [70] H. Noguchi and G. Gompper, “Shape transitions of fluid vesicles and red blood cells in capillary flows,” *PNAS* **102**, 14159–14164 (2005).
- [71] B. Kaoui, G. Biros, and C. Misbah, “Why do red blood cells have asymmetric shapes even in a symmetric flow?” *Phys. Rev. Lett.* **103** (2009).
- [72] J. L. McWhirter, H. Noguchi, and G. Gompper, “Flow-induced clustering and alignment of vesicles and red blood cells in microcapillaries,” *P. Natl. Acad. Sci.* **106**, 6039–6043 (2009).
- [73] B. Klitzman and B. R. Duling, “Microvascular hematocrit and red cell flow in resting and contracting striated muscle,” *Am. J. Physiol.* **237**, H481–H490 (1979).
- [74] B. Klitzman and P. C. Johnson, “Capillary network geometry and red cell distribution in hamster cremaster muscle,” *Am. J. Physiol.* **242**, H211–H219 (1982).
- [75] G. D. O. Lowe, J. C. Barbenel, and C. D. Forbes, *Clinical Aspects of Blood Viscosity and Cell Deformability* (Springer Science & Business Media, 2012).
- [76] J. F. Bertles and P. F. A. Milner, “Irreversibly sickled erythrocytes: a consequence of the heterogeneous distribution of hemoglobin types in sickle-cell anemia,” *J. Clin. Invest.* **47**, 1731–1741 (1968).
- [77] E. T. A. Mohamed, A. E. Kamanyi, M. Pluta, and W. Grill, “Age-dependent acoustic and microelastic properties of red blood cells determined by vector contrast acoustic microscopy,” *Microsc. Microanal.* **18**, 436 (2012).
- [78] A. R. Williams and D. R. Morris, “The internal viscosity of the human erythrocyte may determine its lifespan in vivo,” *J. Haematol.* **24** (1980).
- [79] R. Anderson, M. Cassell, G. L. Mullinax, and H. Chaplin Jr., “Effect of normal cells on viscosity of sickle-cell blood,” *Arch. Intern. Med.* **111**, 286–294 (1963).
- [80] L. Da Costa, J. Galimand, O. Fenneteau, and N. Mohandas, “Hereditary spherocytosis, elliptocytosis, and other red cell membrane disorders,” *Blood Rev.* **27**, 167–178 (2013).
- [81] G. Tomaiuolo, “Biomechanical properties of red blood cells in health and disease towards microfluidics,” *Biomicrofluidics* **8** (2014).
- [82] X. Li, P. M. Vlahovska, and G. E. Karniadakis, “Continuum- and particle-based modeling of shapes and dynamics of red blood cells in health and disease,” *Soft Matter* **9**, 28–37 (2013).
- [83] M. Ulbricht, “Advanced functional polymer membranes,” *Polymer* **47**, 2217–2262 (2006).
- [84] U. Seifert and R. Lipowsky, “Morphology of vesicles,” in *Handbook of Biological Physics*, Vol. 1, edited by R. Lipowsky and E. Sackmann (Elsevier Science B.V., 1995) pp. 403–462.
- [85] A. Guckenberger and S. Gekle, “Theory and algorithms to compute Helfrich bending forces: a review,” *J. Phys. Condens. Matter* (2017).
- [86] L. D. Homer, P. K. Weathersby, and L. A. Kiesow, “Oxygen gradients between red blood cells in the microcirculation,” *Microvasc. Res.* **22**, 308–323 (1981).
- [87] L. D. Homer, J. B. Shelton, and H. McElroy, *The spacing of red cells in the microcirculation during acute anemia*, Tech. Report 55 (Naval Medical Research Institute, 1984).
- [88] P. C. Johnson, “Red cell separation in the mesenteric capillary network,” *Am. J. Physiol.* **221**, 99–104 (1971).
- [89] H. Zhao and E. S. G. Shaqfeh, “The shape stability of a lipid vesicle in a uniaxial extensional flow,” *J. Fluid Mech.* **719**, 345–361 (2013).
- [90] J. B. Dahl, V. Narsimhan, B. Gouveia, S. Kumar, E. S. G. Shaqfeh, and S. J. Muller, “Experimental observation of the

- asymmetric instability of intermediate-reduced-volume vesicles in extensional flow,” *Soft Matt.* **12**, 3787–96 (2016).
- [91] A. Shenoy, C. V. Rao, and C. M. Schroeder, “Stokes trap for multiplexed particle manipulation and assembly using fluidics,” *P. Natl. Acad. Sci.* **113** (2016).
- [92] M. Tanyeri and C. M. Schroeder, “Manipulation and confinement of single particles using fluid flow,” *Nano Lett.* **13**, 2357–2364 (2013).
- [93] T. M. Schneider, S. Mandre, and M. P. Brenner, “Algorithm for a microfluidic assembly line,” *Phys. Rev. Lett.* **106**, 094503 (2011).